COMMUNICATION

Check for updates

Elucidating the role of oxidation in two-dimensional silicon nanosheets†

Jeremy B. Essner, [iD][a] Abhijit Bera, [iD][a] Maharram Jabrayilov, [iD][a] Abhishek Chaudhari, [iD][a] Benjamin T. Diroll, [iD][c] Julia V. Zaikina [iD][b] and Matthew G. Panthani [iD]*[a]

We report a synthetic protocol that yields hydrogen-terminated 2D silicon nanosheets with greatly reduced siloxane (*e.g.*, Si−O−Si, O_xSi) content. These nanosheets displayed weak, broad photoluminescence centered near 610 nm with a low absolute photoluminescence quantum yield (as low as 0.2%). By intentionally oxidizing the nanosheets, the photoluminescence peak emission wavelength blueshifted to 510 nm, and the quantum yield increased by more than an order of magnitude to 8.5%. These results demonstrate that oxidation of 2D silicon nanosheets modulates the material's bandgap and suggests that previously reported photoluminescence properties for this material resulted, in part, from oxidation.

New concepts

A new synthetic route for 2D silicon nanosheets that produces hydrogen-terminated 2D Si with greatly reduced siloxane (*e.g.*, Si–O–Si, O_xSi) content is reported. The 2D silicon nanosheets prepared by this route are effectively non-luminescent with an absolute quantum yield as low as 0.2% while oxidation of the Si monolayers leads to photoluminescent quantum yields over 8%. These results reveal that the photoluminescence previously observed for hydrogen-terminated 2D Si arises from oxidation of the Si backbone, providing a pathway for bandgap engineering in these materials through controlled oxidation.

In the last decade, the demand for computational power, communication, and data storage has skyrocketed. As transistors—the backbone of microelectronic systems—reach their physical size limits and energy consumption continues to rise, alternative methods for information transmission and storage have become critical.[1,2] One promising solution is to use electromagnetic radiation, particularly in the visible to infrared spectrum, as the information carrier. By integrating photonic and optoelectronic devices within microchips, more energy-efficient information transmission could be achieved.[3] However, a significant challenge remains: finding materials that not only emit light efficiently (luminesce) but also integrate seamlessly with current microelectronic infrastructure.[4]

Layered two-dimensional (2D) materials are a rising class of material that display intriguing (photo)physical and electronic properties upon thinning to few-layer stacks of individual monolayers,[5,6] positioning these materials as prime candidates for next-generation photonic and optoelectronic applications. Indeed, since the discovery of graphene in 2004, 2D materials,

such as transition-metal (di)chalcogenides, hexagonal boron nitride, phosphorene, and MXenes, have garnered growing attention in the scientific community as new active materials in photonic and optoelectronics applications, such as quantum emitters/detectors, lasers, light emitting diodes, optical modulators, photovoltaics, and photodetectors, due to their tunable bandgaps, high electrical conductivity, non-linear optics, strong in-plane bonding (*i.e.*, mechanical strength), flexibility, and tailorable surface chemistry.[6–11] While these materials show promise for next-generation photonic and optoelectronic applications, they often suffer from poor, or even non, compatibility with the current microelectronic infrastructure.

As the heart of microelectronics is silicon, materials based on group IV elements are ideal candidates for next-generation photonic and optoelectronic applications due to their complementary metal–oxide semiconductor compatibility, which allows facile integration into current microelectronic infrastructures.[12–16] Unfortunately, the group IV semiconductors possess indirect bandgaps and are, thus, terribly inefficient at emitting light. However, this inefficient luminescence can be overcome by confining at least one physical dimension of the group IV semiconductors to the nanoscale making (luminescent) 2D materials based on group IV elements (*i.e.*, Xenes, Xanes) of keen interest for next-generation photonic and optoelectronic applications, and beyond.[17–25] For example, 2D germanium has been explored in diode and photodetector applications due to

[a] *Department of Chemical and Biological Engineering, Iowa State University, Ames, Iowa 50011, USA. E-mail: panthani@iastate.edu*

[b] *Department of Chemistry, Iowa State University, Ames, Iowa 50011, USA*

[c] *Center for Nanoscale Materials, Argonne National Laboratory, 9700 S. Cass Avenue, Lemont, IL 60639, USA*

† Electronic supplementary information (ESI) available: Experimental details, pXRD, SEM images, EDS analyses, FTIR, PL, TRPL. See DOI: https://doi.org/10.1039/d4nh00387j

its predicted high electron mobility and direct, tunable bandgap.[22,23,26] 2D silicon (*e.g.*, silicene, silicane, siloxene) is of particular interest as the active material in photonic and optoelectronic devices due to its tunable surface chemistry,[27,28] observed photo- and electro-luminescence,[24,29–31] high charge carrier mobilities,[32] and non-linear optical properties.[33] Additionally, 2D silicon has shown promise in numerous other technologies such as batteries,[34] supercapacitors,[35] neuromorphic devices,[36] and biomedical applications.[37] However, before 2D Group IV materials can be successfully deployed in commercial applications, particularly optoelectronic devices, improved understandings of their structure–property relationships and light–matter interactions are required.

Atomically thin, freestanding 2D silicon (111) nanosheets (*e.g.*, silicane) represent an ideal foundation to build these understandings on due to (1) the terrestrial abundance of silicon and (2) the vast library of knowledge that already exists for bulk Si surfaces, such as (111) oriented Si.[28] However, despite freestanding 2D silicon nanosheets (SiNSs) being first reported over 150 years ago,[38] little progress has been made towards such understandings since.[39–44] Further, the sparce work has introduced conflicting conclusions in the literature record on the structural nature of the 2D Si monolayers. Specifically, whether the individual Si monolayers are fully hydrogen terminated (*i.e.*, silicane/layered polysilane),[42–44] 50% hydroxylated (*i.e.*, Wöhler/Weiss siloxene),[38,41] contain siloxanes (*i.e.*, Kautsky siloxene),[39,40] or chlorine termination.[43] This variability in reported structure stems, in part, from the inconsistencies in preparation methods, with materials often being insufficiently characterized when experimental parameters are changed. For instance, these materials are typically prepared from the layered Zintl phase, calcium disilicide ($CaSi_2$), through topotactic deintercalation of Ca^{2+} by (concentrated) aqueous HCl,[39–44] however, the employed $CaSi_2$ purity, atmospheric composition, deintercalation temperature, and product purification vary widely with minimal conclusions drawn in relation to these differing experimental parameters.

Recently, our group provided insight into this long-standing debate by demonstrating that impurities in $CaSi_2$ have impacted interpretation of SiNS structural characterizations and that the 2D Si monolayers consist of a buckled Si backbone terminated with randomly distributed hydrogen, chlorine, and hydroxyl groups in an approximate ratio of 70 : 20 : 10, respectively.[29,45] We note that this assessed surface termination is for SiNSs prepared under inert atmosphere at temperatures below −30 °C. The literature suggests that SiNSs prepared in air or at higher temperatures possess a different ratio of these groups;[43,46] however, exact ratios and correlations to these experimental parameters have yet to be reported. We also demonstrated that, while infrared spectroscopy indicates the presence of siloxanes (Si–O–Si) *via* an intense stretch at approximately 1050 cm^{-1}, the intensity of this mode arises from a relatively large induced dipole moment, not a high concentration of siloxane groups within the material.[29] While the quantity of oxidation within the SiNSs in the form of siloxane is minute, its exact origin (*e.g.*, oxygen, water) and subsequent

impact on observed material properties remains unaddressed. Indeed, the presence of oxidation within the material has only further complicated structure–property understandings, such as the origin of the material's room-temperature, cyan (500 nm) photoluminescence (PL) and PL quantum yields (Φ_{PL}) of nearly 10%.[29,43,47] Historically, the origin of this PL has been attributed to chemical quantum confinement of silicon by oxygen; however, this conclusion has been intensely debated.[48–51]

We previously simulated band structures of fully hydrogen-terminated 2D Si (*e.g.*, $Si_{32}H_{32}$) and various oxidized forms of this parent structure using DFT.[30] Additionally, our collaborators simulated band structures of 2D Si with different ratios of hydrogen and chlorine termination.[45] These studies showed that fully hydrogen-terminated SiNSs possess a quasi-direct band structure with direct and indirect bandgap energies (E_g's) of approximately 2.26–2.1 eV and 2.16–2.05 eV, respectively,[29,30,45] suggesting this material should display weak PL between approximately 550 and 600 nm. Additional simulations of oxidized SiNS structures revealed a shift to a direct bandgap material with an E_g of 2.14 eV (579 nm) upon the formation of only one siloxane group (Si–O–Si) per every 32 Si atoms.[30] Further formation of siloxane groups about a central Si atom (*i.e.*, O_2SiH, O_3SiH) led to slightly lower E_g (<2.11 eV; 588–600 nm), while increased oxidation in other configurations led to inconsistent trends in E_g. However, in all instances, increasing oxidation resulted in direct bandgaps. These previously reported simulations suggest that oxidation of SiNSs will produce a concomitant red shift and increase in PL, relative to fully hydrogen terminated SiNSs, providing a viable route for band structure engineering of these materials *via* controlled oxidation.

Herein, we provide evidence that dissolved oxygen present in the aqueous HCl is the primary source of the oxidation that is observed in freshly prepared, hydrogen-terminated SiNSs (H-SiNSs), thus providing a synthetic route for SiNSs free of siloxane groups (Scheme 1). We must clarify that the H-SiNS composition is nominally $SiH_{0.7}Cl_{0.2}(OH)_{0.1}$ and we only refer to the material as H-SiNSs for simplicity. We found that these H-SiNSs exhibit weak PL ($\Phi_{PL} < 0.6\%$) centered near 610 nm, with this feature attributed to the recently elucidated surface composition for H-SiNSs ($SiH_{0.7}Cl_{0.2}(OH)_{0.1}$), a conclusion that is reinforced by previously reported band structure simulations.[45] Furthermore, we also found that oxidation is responsible for the cyan (500 nm) photoluminescence ($\Phi_{PL} = 8–10\%$) often observed. This conclusion is supported by correlated increases in oxygen content in the material (assessed by FTIR and EDX spectroscopies) and Φ_{PL} (schematically shown in Scheme 1).

Results and discussion

Synthesis of silicon nanosheets

We prepared the calcium disilicide ($CaSi_2$) precursor and deintercalated silicon nanosheets (SiNSs) following our previously reported protocols.[30,52] Comprehensive descriptions of the experimental details are provided in the methods section of the ESI.† Briefly, we synthesized the $CaSi_2$ precursor *via* a
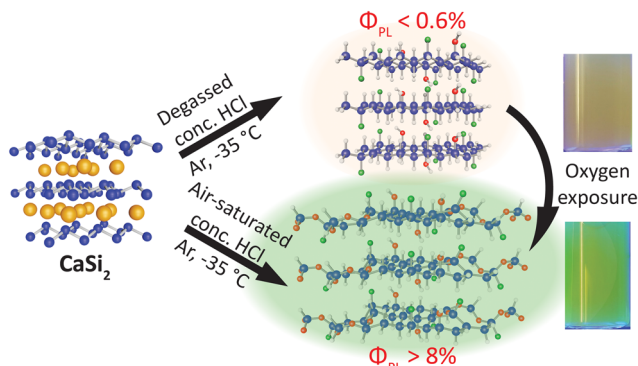
Scheme 1 Deintercalation of the Zintl phase precursor, CaSi$_2$, using degassed HCl yields a weakly red emitting material with a peak PL centered at 610 nm and a photoluminescent quantum yield (Φ_{PL}) as low as 0.2% (highest of 0.6%). Upon oxygen exposure, either in the form of dried air or dissolved gas in the HCl, the photoluminescence effectively "turns on" leading to at least a 14-fold increase in Φ_{PL} to over 8% and a 100 nm blueshift in peak PL to approximately 516 nm.

hydride approach and prepared the SiNSs by deintercalating the CaSi$_2$ with concentrated HCl at -35 °C under inert atmosphere (e.g., Ar).[52] We confirmed the phase purity of the CaSi$_2$ precursor with pXRD (Fig. S1, ESI†). We generated the H-SiNSs by rigorously degassing the HCl prior to the addition of CaSi$_2$; the degassing protocol consisted of bubbling Ar through the HCl for at least 24 h, followed by four freeze–pump–thaw cycles. Additionally, we employed air-free filtration glassware to isolate the SiNSs from the HCl before transferring the glassware assembly to a glovebox filled with nitrogen for further purification. The reproducibility of this approach was confirmed with pXRD, FTIR, and PL measurements (Fig. S2 and S3, ESI†). Lastly, to oxidize the SiNSs, we injected incremental volumes of dried air (see ESI†) into degassed, anhydrous acetonitrile (ACN) dispersions of SiNSs under inert atmosphere and kept the dispersions under magnetic stirring for 48 h. All samples are denoted by the oxygen (O$_2$):Si mole ratio (reported in parts per hundred, pph), where the reported values represent the amount of molecular oxygen intentionally exposed to the SiNSs (0.0, 0.2, 0.5, 1.1, 2.2, 4.4, and 8.4 pph); we use the "pph" nomenclature instead of atom percent to avoid confusion with Φ_{PL} values. Note, the 0.2 pph sample is the sample prepared in air-saturated HCl; see the ESI† for details on how we arrived at this value. We characterized the samples with powder X-ray diffraction (pXRD), Fourier-transform infrared (FTIR) spectroscopy, scanning electron microscopy (SEM), energy-dispersive X-ray (EDS) spectroscopy, and optical spectroscopies, with confirmation of SiNS oxidation achieved with FTIR and EDS. We note that all solvents employed in this work were anhydrous and were degassed prior to use, unless otherwise noted, to minimize unintentional oxidative effects.

Structural characterizations

We assessed the impact of oxygen exposure on the SiNSs' long-range structure with pXRD and SEM. Exposing the SiNSs to increasing quantities of dried air (0.2–8.4 pph O$_2$:Si) led to the

emergence of bimodal diffraction associated with the interlayer nanosheet spacing ($2\theta \approx 13.5°$; (001) peak), which eventually separated into two distinct peaks centered at $2\theta \approx 10°$ and $2\theta \approx 14°$, corresponding to d spacings of approximately 8.3 and 6.3 Å, respectively (Fig. 1(A) and inset). The full diffraction patterns are provided in the ESI† (Fig. S4). Note, we normalized the diffraction patterns to the (001) peak and deconvoluted these patterns between $2\theta = 5$–$20°$ to obtain the d-spacing values (Fig. S5, ESI†). The diffraction peak centered at 6.3 Å for all samples is consistent with previously reported DFT simulations that predicated an interlayer spacing of 6.2 Å for SiH$_{0.7}$Cl$_{0.2}$(OH)$_{0.1}$.[45] Additionally, our previous DFT simulations of thermodynamically relaxed, fully hydrogen-terminated 2D Si with different configurations of Si–O–Si bond formation revealed that oxidation of the SiNS backbone induced structural strain that further buckled the Si network;[30] this buckling impacted atomic configurations (e.g., bond angles) over five Si sites away for just one in 32 Si atoms oxidized to O$_x$SiH (see supporting information of ref. 30). Given this, we tentatively attribute the emergence of the diffraction peak centered near $2\theta \approx 10°$ upon increasing oxygen exposure to buckling of the Si backbone from Si–O–Si bond formation (i.e., oxidation), which increases the interlayer spacing to approximately 8.3 Å. Based on this tentative conclusion, the broadness of the peak
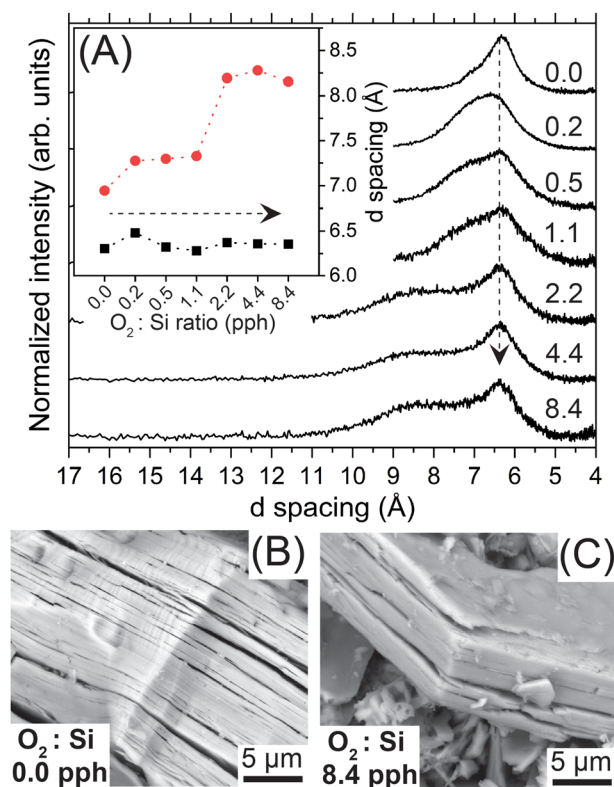
Fig. 1 (A) pXRD of the SiNSs exposed to increasing quantities of oxygen. The d spacing extracted from deconvolution of the pXRD patterns is provided in the inset. The dashed arrows indicate increasing oxygen exposure. Representative SEM images of (B) SiNSs generated in degassed HCl (0.0 pph O$_2$:Si ratio) and (C) SiNSs exposed to the highest quantity of oxygen in this study (8.4 pph O$_2$:Si ratio).

centered at 8.3 Å also suggests a random distribution of O_xSiH groups within the Si backbone, where x = 0–3. Therefore, the bimodal distribution observed for the interlayer spacing indicates that the large sheet stacks consist of non-oxidized SiNSs, nominally of the composition $SiH_{0.7}Cl_{0.2}(OH)_{0.1}$, and SiNSs with a broad range of larger interlayer spacings arising from varying degrees of oxidation of the SiNSs. Even though we mildly exfoliated the SiNSs via bath sonication prior to intentional oxidation and kept the dispersions under magnetic stirring during the oxidation period, the poor dispersibility of these samples hinders complete exfoliation, thus restricting the accessibility of O_2 to the inner most monolayers and resulting in a heterogenous mixture of variably oxidized and non-oxidized 2D Si materials. Lastly, the results show that pXRD can be used as a qualitative gauge for oxidation of SiNSs. That is, observed peak asymmetry, in the form of a shoulder, on the higher d spacing side of the peak at 6.3 Å is indicative of early-stage oxidation of the outer monolayers or monolayer edges/corners.

To assess whether the hypothesized backbone buckling translated to macroscopic changes in the (stacks of) nanosheets, we imaged the SiNS samples with SEM. Representative SEM images of the 0.0 pph O_2:Si sample and the SiNS sample exposed to the highest quantity of oxygen (8.4 pph O_2:Si) are provided in panels (B) and (C) of Fig. 1, respectively. The macroscopic features of the SiNS samples generated in degassed HCl (0.0 pph O_2:Si; Fig. 1(B) and Fig. S6(A), ESI†) are consistent with those observed for samples previously prepared in our lab (i.e., air-saturated HCl (approx. 0.2 pph O_2:Si)).[29,30,45] Conversely, an apparent decrease in nanosheet (stack) size is observed for the sample exposed to the highest quantity of oxygen (Fig. 1(C) and Fig. S6(C), ESI†). A control study, in which the SiNSs prepared in air-saturated HCl (0.2 pph O_2:Si) were bath sonicated in ACN, revealed that the exfoliation of the SiNS stacks during the bath sonication step (Fig. S6(B) and S6(C), ESI†) caused the observed size reduction. The observed size decreases in the sheet stack thickness and nanosheets' lateral dimensions are attributed to improved exfoliation of the sheet stacks between individual monolayers and along grain boundaries that were present in the polycrystalline precursor, respectively. While we currently attribute the origin of the size decrease to the above, we cannot rule out mild sonication providing sufficient energy to cleave the weak Si–Si bonds ($\sim$53 kcal mole^{-1}) of the nanosheet. Regardless, the O_2 exposure explored in this study did not markedly alter the macroscopic structure of the SiNSs (stacks).

We initially confirmed that exposure of the SiNSs to oxygen led to oxidation of the material with SEM-EDS analyses. While the oxygen content cannot be rigorously quantified with EDS due to oxygen in the carbon mounting tab and its ubiquitous presence (in minute quantities), regardless of employing stringent air-free conditions, increasing exposure to molecular oxygen clearly led to increasing oxygen content in the SiNSs (Table S1 and Fig. S7(A), ESI†). Representative SEM images and EDS data that Fig. S7 (ESI†) originates from are provided in Fig. S8 and S9 (ESI†). We also corrected the elemental composition for

both (i) oxygen contributions from the carbon mounting tab using the C:O ratio determined from analysis of a bare mounting tab (Fig. S7(B), ESI†) and (ii) residual calcium chloride ($CaCl_2$) in the sample (Fig. S7(C), ESI†), as this byproduct is frequently observed in samples due to incomplete removal during the washing step.[29,45] The as-collected and corrected values are all tabulated in Table S1 (ESI†). We recognize that such corrections are based on many assumptions, however, the trends observed for the atomic percent (at%) of Si, O, and Cl remain essentially identical throughout these analyses. Therefore, the observed increase and decrease in O and Cl, respectively, are not artifacts of the sample or measurement. We also calculated the Cl:Si atomic ratio to further assess if the observation in decreased Cl is attributable to a real change in chlorine termination and is not a product of the increasing oxygen content (Fig. S7(D), ESI†; we scaled the ratio by a factor of six for improved clarity. For the 0.0 pph O_2:Si sample, the Cl:Si atomic ratio is consistent with previously reported ratios of 1–2 terminating Cl atoms per every 6 Si atoms;[45] however, a correction for residual $CaCl_2$ had not been performed in our previous work. Thus, the corrected Cl:Si atomic ratios that we determined for the 0.2 pph O_2:Si sample produced here and our previous sample[45] are lower than the value we previously reported (approximately 0.8 Cl per 6 Si vs. 1.0 Cl per 6 Si). We note that previous characterizations with solid-state NMR yielded a ratio of 1.2 Cl per 6 Si;[45] in these measurements, residual $CaCl_2$ does not contribute to this ratio. We attribute the discrepancy between EDS and NMR to the brief air exposure (<15 min) that occurred when the previously reported samples were characterized with SEM. Conversely, in this work, we placed the samples in a specially designed sample holder capable of maintaining a controlled environment from a glovebox to within the SEM. Given this difference in sample treatment, the above analysis indicates that Cl termination is rapidly lost upon air (O_2) exposure, consistent with a previous report on the stability of Cl on Si(111).[53] Conversely, chlorinated Si(111) surfaces have been reported to be quite air stable,[54,55] however, partial chlorination and Si–Cl bonds on step edges are more reactive.[55] Therefore, we attribute the observed reactivity of Si–Cl in the SiNSs to the low Cl content and Si–Cl groups present along the edges. The instability of the Si–Cl bonds in the SiNSs is further confirmed by the drop in the Cl:Si atomic ratio to 0.5 Cl per 6 Si upon increasing the O_2:Si ratio to 0.5 pph. Further increasing the O_2:Si ratio to 2.2 and then 8.4 pph did not lead to any additional changes in the Cl:Si atomic ratio. We attribute this trend to the outer most nanosheets within a stack losing their Cl termination while those terminations deep within a stack remain intact due to inaccessibility by O_2; such a conclusion is consistent with the conclusions drawn by pXRD. Overall, these results indicate that chlorine termination is lost during oxidative processes by molecular oxygen. Therefore, we anticipate that the 0.0 pph O_2:Si sample will have an even higher Cl:Si atomic ratio than the previously assessed 1.2 Cl per 6 Si since these samples contained higher levels of oxidation compared to the 0.0 pph O_2:Si sample (as assessed by FTIR); solid-state NMR characterizations are currently underway to confirm this hypothesis.
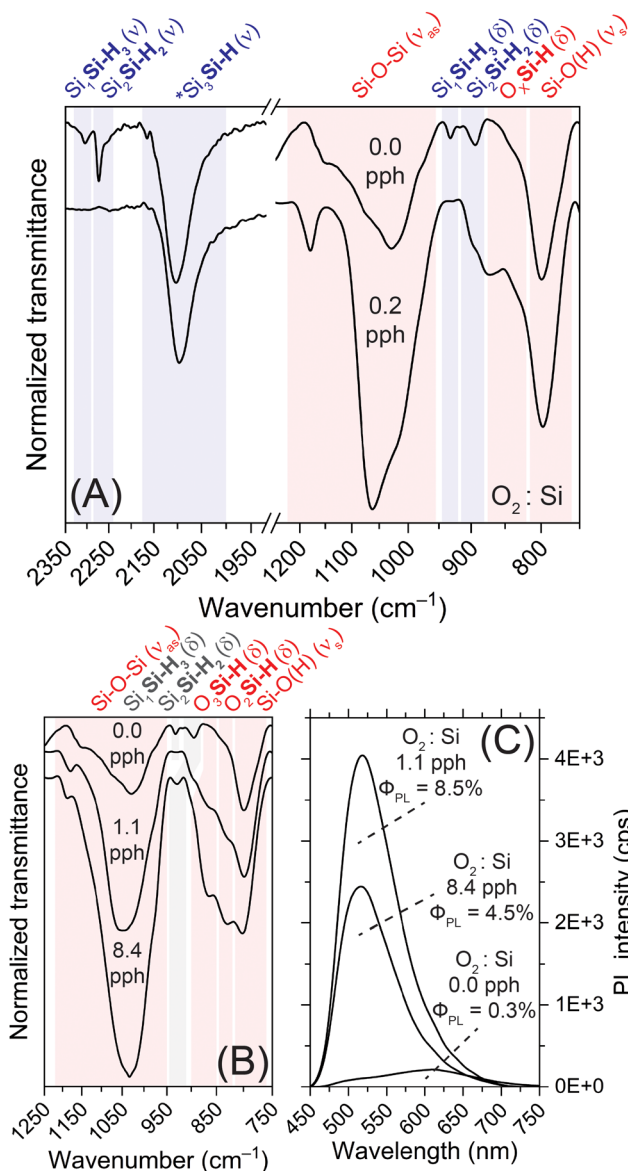
Fig. 2 (A) FTIR spectra of SiNSs prepared in degassed HCl (0.0 pph O_2 : Si) or air-saturated HCl (0.2 pph O_2 : Si). (B) FTIR spectra of select SiNS samples showing changes observed to oxygen-related vibrations upon increasing oxygen exposure. (C) Corresponding PL spectra for the samples shown in panel (B), revealing a marked increase in PL (Φ_{PL} of 0.3% to Φ_{PL} of 8.5%) upon slight oxygen exposure, and, thus oxidation of the Si backbone. *Note, all FTIR spectra were normalized to the Si_3Si-H stretch near 2100 cm^{-1}.

We further characterized the SiNSs with FTIR spectroscopy to confirm oxidation of the SiNSs and better understand the local chemical environment. FTIR spectra highlighting key differences between 0.0 pph O_2 : Si (degassed HCl) and 0.2 pph O_2 : Si (air-saturated HCl) are provided in Fig. 2(A), while spectra highlighting specific $O_xSi(-H)$ vibrational modes for increasing oxygen exposure are provided in Fig. 2(B). Note, spectra of the full wavenumber range collected are provided in Fig. S10(A) (ESI†). In general, the FTIR spectral profiles are consistent with previous samples generated in our lab, where

the SiNS surface consists of –H, –OH, and –Cl functionalities.[29,30,52] Specifically, Si–H stretching for Si bonded to three other Si atoms near 2100 cm^{-1}, Si–H stretching for Si bonded to at least one oxygen atom on the red-edge shoulder of the 2100 cm^{-1} peak, Si–H stretching for Si bonded to three oxygen atoms at approximately 2200 cm^{-1}, Si–O–Si asymmetric stretching between 950–1200 cm^{-1}, Si–H bending, including SiH_3/SiH_2, at approximately 900 cm^{-1}, 670 cm^{-1}, 630 cm^{-1}, and 512 cm^{-1}, O_xSiH bending between 810–910 cm^{-1}, Si–O symmetric stretching (including Si–O within Si–OH) at 800 cm^{-1}, O–H stretching from Si–OH at approximately 3600 cm^{-1}, and a Si–Cl vibration at 570 cm^{-1}. Our previous DFT simulations support these assignments.[29] The key differences between the 0.0 pph O_2 : Si (degassed HCl) and 0.2 pph O_2 : Si (air-saturated HCl) samples, as well our previously published results,[29,30] are the intensity and spectral shape of the Si–O–Si asymmetric stretch, as well as the observance of vibrations ascribed to SiH_3 and SiH_2 stretching (2250–2350 cm^{-1}) and bending (875–950 cm^{-1}) modes; these differences indicate that SiH_3 features, and to a lesser extent SiH_2, quickly oxidize upon oxygen exposure. The reproducibility of these features for different 0.0 pph O_2 : Si samples is highlighted in panels (B) and (C) of Fig. S3 (ESI†). Further increasing the oxygen exposure resulted in the following changes to Si–O vibrations: (i) the asymmetric stretch of Si–O–Si (approximately 1050 cm^{-1}) markedly increased, (ii) two peaks between 810–910 cm^{-1} from O_xSiH bending grew in, and (iii) a weak vibration near 2250 cm^{-1} from Si–H stretching of O_3SiH emerged (Fig. 2(B), 3(A), 3(B) and Fig. S10(A), ESI†). Additionally, spectral shifts in peaks arising from Si–H stretching and bending are observed (Fig. S10(B), ESI†), changes that are consistent with increasing oxidation and decreasing Cl termination.[56,57] Note, the vibrations centered near 3400 and 1650 cm^{-1} arise from adsorbed water, not –OH surface termination, features often misassigned in the literature. Additionally, any observed CH_x stretching is attributed to residual organic solvent on the ATR crystal after cleaning, as CH_x stretching is not always observed. In the case of the 0.0 pph O_2 : Si sample, however, the observed CH_x stretching arises from the mineral oil that we immersed the sample in to minimize potential oxidation during data collection (<30 s air exposure prior to collection; <5 min total air exposure). As all other samples were exposed to air during data collection, we conducted a time-dependent FTIR study of the 0.0 pph O_2 : Si sample not immersed in oil (Fig. S11(A), ESI†). This study revealed that rapid, albeit minor, oxidation of the SiNSs occurred within 30 s of air exposure; however, we did not observe further oxidation *via* FTIR after an additional 15 min of air exposure. Even after 48 h of wet air exposure in a capped vial, the sample remained less oxidized than the sample generated in air-saturated HCl (0.2 pph O_2 : Si sample). Further, the minor spectral shifts observed in Si–H stretching and bending modes are consistent with slight oxidation (Fig. S11(B), ESI†). Thus, the results show that the brief air exposure that occurred during data collection is unlikely to result in a measurable level of oxidation in samples already partially oxidized. Additionally, the results indicate that once the SiNSs are partially oxidized they are relatively stable in powder form. Lastly, the intensity of the Si–Cl vibration weakened slightly with increasing
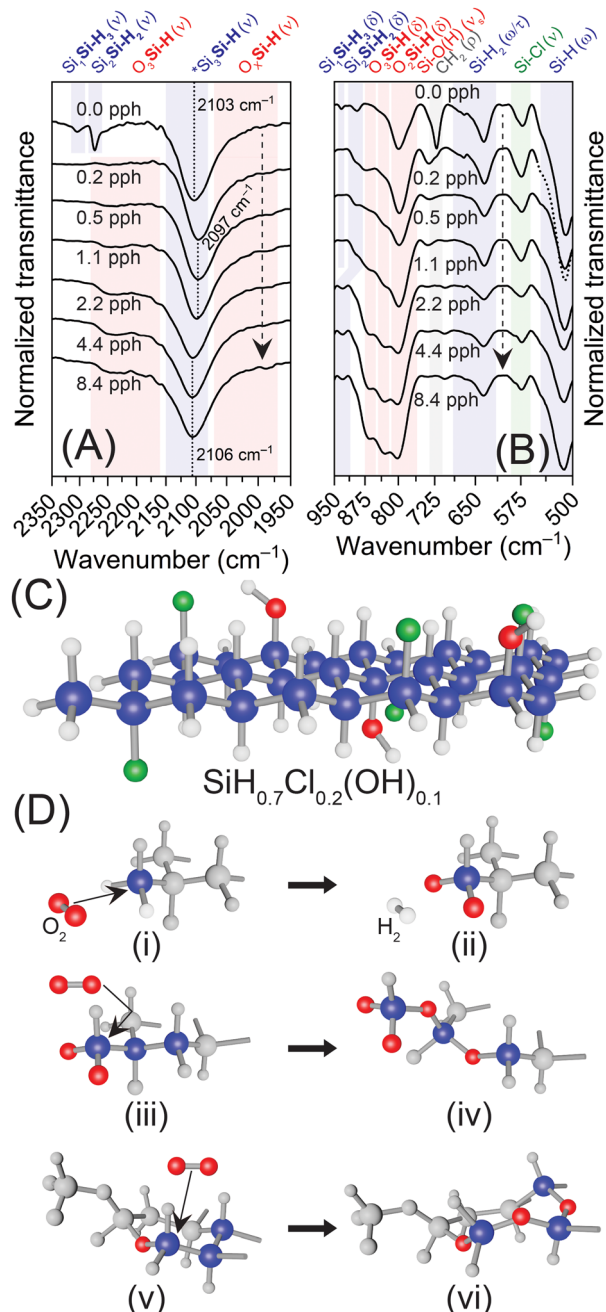
Fig. 3 (A) and (B) FTIR spectra of SiNS samples exposed to increasing quantities of dried air; panel (A) highlights the changes to $Si_{3-x}Si-H_{1+x}$ vibrations while panel (B) focuses on changes in $Si-H_x$ bends and the Si–Cl vibration. The dashed arrows indicate increasing oxygen exposure. *Note, all FTIR spectra were normalized to the Si_3Si-H stretch near 2100 cm^{-1}. Also, the portion of the spectrum for the 0.2 pph O_2 : Si sample plotted as a dashed line in panel (B) is done so solely for clarity. (C) Structural schematic of SiNSs with nominally 70% hydrogen (white), 20% chlorine (green), and 10% hydroxyl (red & white) surface terminations ($SiH_{0.7}Cl_{0.2}(OH)_{0.1}$). (D) Schematic of the proposed oxidation mechanism showing: (i) the initiating oxidative event *via* reaction of O_2 with an SiH_3 group forming (ii) O_2SiH, (iii) oxidative attack of the formed O_2Si group in (ii) leading to (iv) oxygen insertion into the Si backbone, and (v) and (vi) propagation of Si–O–Si and O_2Si through the backbone with repeated oxygen exposure. Note: non-participating atoms in each step are grayed out for clarity.

oxygen exposure, suggesting a loss of chlorine termination (Fig. S10(A), ESI†), which is consistent with our conclusions from the EDS analyses.

Optical and optoelectronic properties (PL, Φ_{PL})

We then characterized the SiNSs with steady-state photoluminescence spectroscopy, absolute Φ_{PL} measurements, and time-resolved photoluminescence to elucidate the impact of the aforementioned chemical and structural changes on material properties. Most notably, the sample prepared in degassed HCl (0.0 pph O_2 : Si) displays completely different PL characteristics (spectral profile, peak position, Φ_{PL}) than previously reported PL features for SiNSs (Fig. 2(C) and Fig. S12, ESI†).[29,30,47] Specifically, this sample presents weak, broad PL centered near 610 nm with an absolute Φ_{PL} as low as 0.2% (Fig. 2(C)), a full-width at half maximum (FWHM) of 160 nm, and a base width of 350 nm. The breadth of this peak indicates that this material possesses a broad distribution of states. The reproducibility of the PL is highlighted in Fig. S3(D) (ESI†). While minor differences in intensity are observed (Φ_{PL} of 0.3–0.6%), a correlation between the extent of oxidation and Φ_{PL} was not apparent at these low levels of oxidation. Thus, we attribute the differences in PL intensity to a combination of varying levels of (i) oxidation (undetectable by FTIR) and (ii) sample suspended in the excitation source; although standardized preparation protocols were employed, the poor dispersibility of these samples and their intense scattering nature lead to variability in solvent-based measurements. Conversely to the degassed HCl samples, when the SiNSs were prepared in air-saturated HCl (0.2 pph O_2 : Si), the PL intensity increased substantially ($\Phi_{PL} \approx$ 4–5%) and the peak maximum blueshifted to 520 nm (Fig. S12(A), ESI†). Additionally, exposure to this minute quantity of oxygen markedly decreased peak broadness (FWHM of 80 nm; 250 nm base width), indicating a reduction in distribution of states; similar spectral features were observed for other oxidized samples (Fig. S12(A), ESI†). Further increasing the quantity of oxygen exposure led to even higher PL intensity up to 1.1 pph O_2 : Si (Φ_{PL} = 8.5%; Fig. 2(C)), after which the PL intensity decreased and blueshifted further. Specifically, for the highest O_2 : Si ratio tested (8.4 pph O_2 : Si), the PL peak maximum shifted to 516 nm and the absolute Φ_{PL} decreased to 4.5% (Fig. 2(C)); this decrease is attributed to increasing SiO_2 character.

To better understand these observations in the context of previous results, we compared the FTIR and steady-state PL spectra of the SiNSs prepared in degassed (0.0 pph O_2 : Si) and air-saturated (0.2 pph O_2 : Si) HCl to samples previously generated in our lab (Fig. S12(B) and S12(C), ESI†);[29,30] the peak PL and FWHM values were extracted from all PL spectra and are provided in Fig. S12(D) (ESI†). These data show that the extent of oxidation varies greatly between these samples and the PL from previous samples is blueshifted relative to all samples explored in this work. While no clear trends emerged between the different samples, we do note the spectral shape of all the samples prepared in air-saturated HCl (0.2 pph O_2 : Si) is highly consistent. Despite this, the lack of correlations between the extent of apparent oxidation and peak PL for samples explored

herein and previous samples suggests that there is another factor impacting PL that must be considered. One key difference between the samples in this work and our previous works is that the samples in the latter were washed with and dispersed in methanol (MeOH) for $CaCl_2$ removal and characterization, respectively.[29,30,45] Given that Si–halide groups can react with alcohols (R-OH) to produce Si-OR,[58,59] we hypothesize that these differences are related to the formation of methoxy groups on the nanosheet surface.

We also characterized the SiNSs with room temperature time-correlated single photon counting and spectrally and time-resolved photoluminescence (Fig. S13, Tables S2, S3, ESI†). For all samples, the PL consists of a multicomponent decay with approximately 93% of the PL intensity decaying in under 30 ns, suggesting that the PL could arise from a direct bandgap transition. This rapid decay coupled with minimal contributions from the longer-lived component makes comparison of changes in direct vs. indirect character challenging. However, the general trends observed between the two measurements for increasing oxygen exposure are fairly consistent; the decay rate for the long-lived component first slows for slight oxygen exposure (1.1 pph O_2:Si) but again increases upon further oxygen exposure (8.4 pph O_2:Si). These trends suggest that increasing oxidation introduces more direct bandgap behavior, which is consistent with previous band structure simulations that demonstrated increasing oxidation (Si_3**SiH** to O_1Si_2**SiH** to O_3**SiH**; the bolded Si atoms are the central atom) shifted the band structure to direct.[30] We conducted the time-correlated single photon counting measurements in both ACN and MeOH and the decays were fit to a tri-exponential function, for direct comparison to literature;[29] the lifetimes and contributions for each component are provided in Table S2 (ESI†). For samples dispersed in ACN, clear trends emerge with increasing oxygen exposure: (i) the contributions from the fastest component (τ_1) increase and (ii) the contributions for the two slower components (τ_2 and τ_3) both decrease. These trends coupled with the marked increase in Φ_{PL} for the oxidized SiNSs relative to the 0.0 pph O_2:Si sample suggests an increase in direct bandgap behavior. We note that, despite the observed increase in Φ_{PL}, the Φ_{PL} values are relatively low indicating the excited state depopulation is still dominated by non-radiative processes. Interestingly, the lifetimes for the sample prepared in degassed HCl (0.0 pph O_2:Si) are markedly shorter than all samples exposed to oxygen, which we tentatively attribute to the weaker PL from this sample at the wavelength monitored (510 nm; see Fig. 2(C)). Contrary to the ACN dispersions, a marked reduction in the lifetime of the third component occurred for MeOH-dispersed samples with increasing oxygen exposure, which suggests an increase in direct bandgap character, although the relatively consistent contributions do not support this. We note that the lifetime values and contributions for MeOH dispersions are consistent with those reported in literature;[29] however, these values were for a sample with higher oxidization, based on the relative Si–O–Si vibration in FTIR (Fig. S12(B), ESI†). Further, this sample displayed a Φ_{PL} of 9%, indicating that the photophysics are being influenced by

yet another factor other than oxidation, such as the formation of methoxy (CH_3O-) termination.

To better understand how the various components contribute to the spectral profile, we integrated the spectrally and time-resolved PL counts for select samples (0.0, 1.1, and 8.4 pph O_2:Si) as a function of time range (Fig. S14, ESI†). For all samples, the decays are dominated by fast (<5 ns) but spectrally broad PL from 400 to nearly 800 nm, suggesting a broad distribution of direct states. For the 0.0 pph O_2:Si sample (Fig. S14(A) and S14(B), ESI†), the PL peaks of the short-lived contributions are centered near 570 nm while the peaks of the weaker, longer-lived contributions (0.2–20 µs) are centered near 610 nm. For the 1.1 pph O_2:Si sample (Fig. S14(C) and S14(D), ESI†), the PL peak of the short- and long-lived contributions are centered near 550 nm, while for the 8.4 pph O_2:Si sample, the PL peak blueshifts further to approx. 520 nm (Fig. S14(E) and S14(F), ESI†). Additionally, the long-lived contributions for the 8.4 pph O_2:Si sample essentially disappear, consistent with oxidation increasing direct bandgap character. These trends are also consistent with conclusions drawn from pXRD. That is, the outermost monolayers within a nanosheet stack and all edges/corners are oxidized first, leaving non-oxidized monolayers near the center of the stacks, which leads to, at minimum, a bimodal distribution of chemically distinct, photoluminescent materials; the parent $SiH_{0.7}Cl_{0.2}(OH)_{0.1}$ and oxidized versions. Based on this, we tentatively attribute the long-lived PL observed on the far red-edge for the 0.0 pph O_2:Si sample to radiative trap states (i.e., dangling bonds) that are passivated upon exposure to oxygen, as these features are not observed in samples exposed to dried air. These conclusions are further supported by the inset panel of Fig. S12(A) (ESI†), where the normalized steady-state PL for the 0.0, 0.2 1.1, and 8.4 pph O_2:Si show (i) overlapping contributions centered near 510 nm which are attributed to oxidized nanosheets, (ii) overlapping contributions centered near 610 nm which are attributed to non-oxidized nanosheets, and (iii) an extended red-edge tail that is only present in the 0.0 pph O_2:Si sample.

Although we fit the PL decays to triexponentials assuming a simple model of a direct radiative channel, a radiative trap state, and a non-radiative trap state, the true electronic structure model is much more complicated. As the above results show, the 2D Si consists of two chemically distinct populations; one very close to $SiH_{0.7}Cl_{0.2}(OH)_{0.1}$ and another of variable oxidation, $O_xSiH_{0.7-y}Cl_{0.2-z}(OH)_{0.1}$. Therefore, we tentatively attribute the fast and slow decay on the blue edge to bimolecular recombination and Shockley–Read–Hall (SRH) recombination, respectively, arising from oxidized nanosheets ($O_xSiH_{0.7-y}Cl_{0.2-z}(OH)_{0.1}$), and the fast and the slow decay on the red edge to bimolecular recombination and SRH or surface recombination, respectively, in the non-oxidized nanosheets, $SiH_{0.7}Cl_{0.2}(OH)_{0.1}$. As our previous report showed that nanosheets possess Si dangling bonds and these silyl radicals behave as midgap states,[30] the decrease in the long-lived component on the red edge upon oxygen exposure and subsequent nanosheet oxidation indicates that oxygen has passivated these surface trap states. Therefore, oxidation results in two changes to the

electronic structure: (i) the band structure switches from quasi-direct to direct, either due to chemical quantum confinement[48–51] or conformational changes,[60–62] and (ii) passivation of surface trap midgap states, both of which reduce the quantity of excited state relaxation through non-radiative channels. That said, as we only conducted room temperature measurements, concrete conclusions cannot be drawn about how the decay kinetics and previously simulated band structures correlate.

To reach a better understanding of these trends and contributions, we compared the experimentally observed PL peak wavelengths to simulated E_g's from our previous works (Fig. S15, ESI†).[29,30,45] As we previously concluded that the surface termination of SiNSs prepared under conditions comparable to those reported herein is best represented by $SiH_{0.7}Cl_{0.2}(OH)_{0.1}$ and previous DFT simulations suggest a direct bandgap with E_g of 1.68 eV (738 nm),[45] the experimental observation of peak PL near 2.03 eV (610 nm) suggests an approximate 0.35 eV discrepancy between the simulated and experimental values. Indeed it is known that DFT underestimates E_g's.[63,64] Operating under the assumption that this discrepancy remains constant for all samples, we adjusted our previously reported E_g's by 0.35 eV for the direct and indirect gaps of fully hydrogen-terminated SiNSs,[29,30,45] as well as the direct gaps of the various oxidized structures.[30] This adjustment revealed (i) that the experimentally observed PL peak for the oxidized samples (2.40 eV; 517 nm) lines up well with the predicted E_g for the previously studied structure with the highest oxidation, $Si_{30}H_{29}(OH)_1O_3$ (2.41 eV; 514 nm), suggesting that oxidation of the silicon backbone is occurring about Si–OH groups, and (ii) that oxidation of fully hydrogen-terminated SiNSs would slightly redshift the PL to approximately 515 nm (lowering of E_g), which is consistent with our previous band structure simulations.[30]

Proposed oxidative mechanisms

The oxidative source (*i.e.*, O_2 *vs.* H_2O) and associated mechanisms for the oxidation of hydrogen-terminated Si surfaces, such as Si(100) and Si(111), have been rigorously investigated,[65–68] with literature suggesting that oxidation by molecular oxygen is initiated and propagated by radical reactions,[66] that result in oxygen insertion between Si–Si bonds forming back-bonded siloxanes.[66–68] Although bulk Si(111) surfaces often provide a robust model for comparison to SiNSs—indeed, the Si backbone of the monolayers possesses the same structure—such comparisons have their limitations, especially in relation to surface chemistry (reactions). That is, Si(111) surfaces are effectively of infinite thickness and contain very few SiH_{1+x} groups, whereas SiNSs are monolayers with surface terminations on both sides and a plethora of SiH_{1+x} groups along the periphery of the monolayers. Indeed, Chabal and coworkers demonstrated that the kinetics of oxidation were faster for a dihydride defect on a Si(111) surface over a defect-free, monohydride Si(111) surface.[67] Therefore, we propose an oxidative mechanism based on increasing reactivity of SiH_x towards oxygen; that is, $SiH_3 > SiH_2 > SiH$. In such a mechanism, the oxygen attacks the SiH_3/SiH_2 groups on the corners/edges of the SiNSs, liberating hydrogen and forming surface Si–O

groups on the sheet periphery (not "bridged" surface siloxanes), followed by an inward propagation of oxidation towards the monolayer center (Fig. 3). Such a mechanism is supported by experimental results provided herein and our previous computational works.[29,30,45] Note, the structures provided in Fig. 3 and Fig. S16 (ESI†) are not thermodynamically relaxed structures; the structures are simply schematic representations of the proposed surface termination and oxidative mechanisms. In the sample generated in degassed HCl (0.0 pph O_2 : Si), three peaks are observed for Si–H vibrations (Fig. 2(A), 3(A) and Fig. S3(B), ESI†) which are assigned to Si–H stretching of $SiSi–H_3$, (2305 cm^{-1}), $Si_2Si–H_2$ (2272 cm^{-1}), and $Si_3Si–H$ (2100 cm^{-1}). As oxygen exposure increased (*i.e.*, air-saturated HCl (0.2 pph O_2 : Si)), the vibrations assigned to $Si_{3-x}SiH_{1+x}$ disappear and the $Si_3Si–H$ vibration red-shifts due to increasing O_xSiH vibrations (Fig. 3(A)). With further oxygen exposure, the peak then blue shifts due to the formation of O_3SiH sites. The loss of SiH_3 and SiH_2 groups *via* hydrogen liberation and subsequent increase in O_xSi sites is further supported by (i) the loss of the $SiSi–H_3$ deformation mode at 932 cm^{-1}, (ii) the decrease in SiH_2 wagging/twisting between 500–750 cm^{-1}, and (iii) the increase in Si–O–Si asymmetric stretching at 1050 cm^{-1} and O_xSiH bending between 810–910 cm^{-1} (Fig. 3(B)). The symmetric stretching of Si–O observed around 800 cm^{-1} is attributed to both the Si–O present in Si–OH and Si–O formed on the sheet edges/corners upon initial stages of oxidation; the latter is evidenced by the slight increase in the intensity of this vibration with increasing oxygen exposure. Although this increase could be ascribed to insertion of oxygen in between Si–H to form Si–OH, the lack of an increasing stretch for Si–OH at approximately 3600 cm^{-1} with increasing oxidation indicates this does not occur. Furthermore, it is well established in the literature that oxygen atoms do not insert between Si and H to form Si–OH groups on hydrogen-terminated Si surfaces.[66–68] Thus, the experimental evidence indicates that oxidation initiates along the sheet periphery through the reaction of molecular oxygen with SiH_3 groups (Fig. 3(C) and 3(D)-i, ii); a similar reaction occurs with SiH_2 edge groups once all SiH_3 corner groups are oxidized (Fig. S16(A), ESI†). Oxidation then propagates inward through the formation of Si–O–Si "chains" *via* oxygen insertion into the Si network (*i.e.*, "backbonding"), forming O_2Si in the process (Fig. 3(D)-iii, vi). Given enough oxygen, O_1Si and O_2Si then oxidize to O_3Si.

These conclusions are further supported by our previous DFT simulations.[29,30,45] Our previous work predicted that bridging oxygens on the surface led to a shift in and broadening of the mode near 500 cm^{-1} due to emergence of additional vibrations between 500 and 600 cm^{-1}, as well as between 700 and 800 cm^{-1}, depending on which Si atoms are bridged (1–2 bridge *vs.* 1–3 bridge).[30] Neither of these scenarios were observed experimentally in this work. Conversely, in our previous DFT simulations, oxygen inserted between Si bonds led to the emergence of multiple modes between 800–1100 cm^{-1}, where the specific vibrations and relative intensities depend on (i) the quantity of oxygen inserted (1 to 3), (ii) the position inserted (about the same or neighboring Si atoms), and (iii) the geometric symmetry around the Si atoms (*i.e.*, 3 inserted oxygen).[30] Given the appearance and subsequent increase of

modes at 830, 865, and 1030 cm^{-1} in the experimental data with no new modes appearing below 800 cm^{-1}, our previous DFT simulations support oxidation of SiNSs arising from oxygen insertion and not surface bridging, a conclusion further supported by oxygen insertion being energetically favorable over the formation of surface siloxanes.[30] Additionally, our previous DFT simulations predicted that it is enthalpically favorable to oxidize a Si atom bonded to at least one oxygen atom over an non-oxidized Si atom, supporting an oxidative propagation of Si–O–Si "chains" followed by subsequent oxidation to higher oxides (i.e., O$_x$Si).

While the current evidence supports a mechanism based on SiH$_x$ reactivity, as the results also demonstrate a loss in chlorine termination (Fig. S7(D) and S10(A), ESI†), the reaction of oxygen with Si–Cl as an initiating event cannot be ruled out (Fig. S16(B), ESI†). Additionally, as our previous DFT simulations predicted that oxidation of O$_x$Si is energetically favorable,[30] the oxidation of Si atoms with hydroxyl termination as the initiating event also cannot be ruled out at this time (Fig. S16(C), ESI†). Indeed the aforementioned consistency in E_g (2.40 eV vs. 2.41 eV) between the intentionally oxidized samples and previously simulated oxidized nanosheets, Si$_{30}$H$_{29}$(OH)$_1$O$_3$,[30] (2.40 eV vs. 2.41 eV; 514 nm), suggests that the Si–OH groups in the material are a key source for oxygen ingress into the backbone, with oxidation concentrating about Si–OH groups in the form of O$_3$SiOH. Lastly, silyl radicals on the sheet edges/corners as the initiating event and propagating mechanism could also occur.[66] Such a mechanism is supported by the loss of long-lived red PL observed in the PL measurements for oxidized samples. Further work is in progress to decouple these potential pathways and mechanistically understand the origin and propagation of oxidation through H-SiNSs.

Conclusions

We present a synthetic approach that yields hydrogen-terminated SiNSs with a structure that is closer to silicane than any previously reported (i.e., decreased siloxane content). These effectively non-oxidized SiNSs exhibit weak, broad PL centered near 610 nm with an absolute Φ_{PL} as low as 0.2%, which is a marked deviation from the previously reported photoluminescence (500 nm; Φ_{PL} = 9%). As our current synthetic protocols employ rigorously air-free preparations, the results clearly indicate that the minor oxidation (assessed by the appearance of Si–O(–Si) (a)symmetric stretching in FTIR) often observed for this material (i.e., silicane, siloxene, layered polysilane) mainly arises from dissolved oxygen in the aqueous HCl that is used during deintercalation of the CaSi$_2$ precursor. Additionally, oxidation of the SiNS backbone is, in part, responsible for the commonly reported cyan (500 nm) PL. Indeed, the PL properties reported here for various levels of oxidized SiNSs explain the inconsistencies reported in the literature for SiNS PL; even in our own lab, we have observed the peak PL of freshly deintercalated SiNSs vary by as much as 30–40 nm (approximately 490 to 530 nm), which we attribute to varying degrees of oxidation that occurs when preparing samples.

Furthermore, we show that exposure of the SiNSs to oxygen, leading to oxidation of the material, does not result in changes to the macroscopic structure but does impact the SiNS surface chemistry and backbone such that noteworthy changes in photoluminescence arise. Specifically, exposure to oxygen results in the loss of H-and Cl- terminal groups, the formation of O$_x$Si networks, and passivation of dangling bonds. These chemical changes result in: (i) an increase the direct bandgap character of and (ii) a reduction in midgap states in 2D Si, evidenced by an increase in Φ_{PL} and a shift in peak PL accompanied by a decrease in long-lived red emission. The trends observed in the PL are consistent with anticipated trends based on previous band structure simulations.[30] Historically, this PL has been attributed to chemically quantum confined silicon via the formation of an extensive Si–O–Si networks;[48–51] however, our experimental results here, combined with our previous band structure simulations, suggest that the buckling of the Si structure upon oxidation[30] leads to a pseudo-conformation change from armchair- to boat-like that may increase the direct bandgap character.[60–62] Lastly, our results reveal that oxidation provides an avenue for tuning bandgap in 2D Si, positioning this material ever closer to commercial application as the active layer in next-generation photonic and optoelectronic devices. However, as oxidation of the Si backbone does not fully account for previously observed PL properties, other strategies can be used to tune the bandgap (e.g., methoxy termination). Further work is underway to elucidate the exact structural composition of the non-oxidized SiNSs and decouple the PL contributions from oxidized and non-oxidized SiNSs (e.g., direct/indirect, methoxy termination).

Author contributions

Jeremy B. Essner: conceptualization, methodology, investigation, validation, data curation, formal analysis, visualisation, and writing – initial draft, review, and editing; Abhijit Bera: investigation, data curation, and writing – review and editing; Maharram Jabrayilov: investigation, data curation, and writing – review and editing; Abhishek Chaudhari: investigation, data curation, and writing – review and editing; Benjamin T. Diroll: resources, supervision, and writing – review and editing; Julia V. Zaikina: resources, supervision, and writing – review and editing; Matthew G. Panthani: funding, resources, conceptualization, project administration, supervision, visualization, and writing – initial draft, review, and editing.

Data availability

Conflicts of interest

There are no conflicts to declare.

Acknowledgements

Notes and references

1 M. Lundstrom, *Science*, 2003, **299**, 210–211.
2 H.-S. P. Wong and S. Salahuddin, *Nat. Nanotechnol.*, 2015, **10**, 191–194.
3 M. Hochberg and T. Baehr-Jones, *Nat. Photonics*, 2010, **4**, 492–494.
4 G. T. Reed, G. Mashanovich, F. Y. Gardes and D. J. Thomson, *Nat. Photonics*, 2010, **4**, 518–526.
5 S. Z. Butler, S. M. Hollen, L. Cao, Y. Cui, J. A. Gupta, H. R. Gutiérrez, T. F. Heinz, S. Sae Hong, J. Huang, A. F. Ismach, E. Johnston-Halperin, M. Kuno, V. V. Plashnitsa, R. D. Robinson, R. S. Ruoff, S. Salahuddin, J. Shan, L. Shi, M. G. Spencer, M. Terrones, W. Windl and J. E. Goldberger, *ACS Nano*, 2013, **7**, 2898–2926.
6 G. R. Bhimanapati, Z. Lin, V. Meunier, Y. Jung, J. Cha, S. Das, D. Xiao, Y. Son, M. S. Strano, V. R. Cooper, L. Liang, S. G. Louie, E. Ringe, W. Zhou, S. S. Kim, R. R. Naik, B. G. Sumpter, H. Terrones, F. Xia, Y. Wang, J. Zhu, D. Akinwande, N. Alem, J. A. Schuller, R. E. Schaak, M. Terrones and J. A. Robinson, *ACS Nano*, 2015, **9**, 11509–11539.
7 Y. Meng, H. Zhong, Z. Xu, T. He, J. S. Kim, S. Han, S. Kim, S. Park, Y. Shen, M. Gong, Q. Xiao and S.-H. Bae, *Nanoscale Horiz.*, 2023, **8**, 1345–1365.
8 P. Vishnoi, K. Pramoda and C. N. R. Rao, *ChemNanoMat*, 2019, **5**, 1062–1091.
9 J. An, X. Zhao, Y. Zhang, M. Liu, J. Yuan, X. Sun, Z. Zhang, B. Wang, S. Li and D. Li, *Adv. Funct. Mater.*, 2022, **32**, 2110119.
10 Z. Cheng, R. Cao, K. Wei, Y. Yao, X. Liu, J. Kang, J. Dong, Z. Shi, H. Zhang and X. Zhang, *Adv. Sci.*, 2021, **8**, 2003834.
11 M. Ghosh Dastidar, I. Thekkooden, P. K. Nayak and V. Praveen Bhallamudi, *Nanoscale*, 2022, **14**, 5289–5313.
12 S. Al-Kabi, S. A. Ghetmiri, J. Margetis, T. Pham, Y. Zhou, W. Dou, B. Collier, R. Quinde, W. Du, A. Mosleh, J. Liu, G. Sun, R. A. Soref, J. Tolle, B. Li, M. Mortazavi,

H. A. Naseem and S.-Q. Yu, *Appl. Phys. Lett.*, 2016, **109**, 171105.
13 R. Soref, *IEEE J. Sel. Top. Quantum Electron.*, 2006, **12**, 1678–1687.
14 R. Soref, *Nat. Photonics*, 2010, **4**, 495–497.
15 D. Thomson, A. Zilkie, J. E. Bowers, T. Komljenovic, G. T. Reed, L. Vivien, D. Marris-Morini, E. Cassan, L. Virot, J.-M. Fédéli, J.-M. Hartmann, J. H. Schmid, D.-X. Xu, F. Boeuf, P. O'Brien, G. Z. Mashanovich and M. Nedeljkovic, *J. Opt.*, 2016, **18**, 73003.
16 S. Shekhar, W. Bogaerts, L. Chrostowski, J. E. Bowers, M. Hochberg, R. Soref and B. J. Shastri, *Nat. Commun.*, 2024, **15**, 751.
17 M. Galbiati, N. Motta, M. De Crescenzi and L. Camilli, *Appl. Phys. Rev.*, 2019, **6**, 41310.
18 G. Shan, H. Tan, R. Ma, H. Zhao and W. Huang, *Nanoscale*, 2023, **15**, 2982–2996.
19 L. C. Lew Yan Voon, E. Sandberg, R. S. Aga and A. A. Farajian, *Appl. Phys. Lett.*, 2010, **97**, 163114.
20 R. Soref, D. Buca and S.-Q. Yu, *Opt. Photonics News*, 2016, **27**, 32–39.
21 O. Olorunsola, A. Said, S. Ojo, H. Stanchu, G. Abernathy, S. Amoah, S. Saha, E. Wangila, J. Grant, S. Acharya, L. Miller, K. Rosler, Y. T. Jheng, G. E. Chang, B. Li, G. Salamo, S. Q. Yu and W. Du, *J. Phys. D. Appl. Phys.*, 2022, **55**, 443001.
22 D. Sciacca, M. Berthe, B. J. Ryan, N. Peric, D. Deresmes, L. Biadala, C. Boyaval, A. Addad, O. Lancry, R. Makarem, S. Legendre, D. Hocrelle, M. G. Panthani, G. Prévot, E. Lhuillier, P. Diener and B. Grandidier, *Nanomaterials*, 2022, **12**, 1128.
23 C. Livache, B. J. Ryan, U. Ramesh, V. Steinmetz, C. Gréboval, A. Chu, T. Brule, S. Ithurria, G. Prévot, T. Barisien, A. Ouerghi, M. G. Panthani and E. Lhuillier, *Appl. Phys. Lett.*, 2019, **115**, 52106.
24 B. J. Ryan, B. T. Diroll, Y. Guo, C. J. Dolgos, Q. H. Wang, L. T. Roling and M. G. Panthani, *ECS Trans.*, 2021, **102**, 3.
25 M. S. Ferris, A. P. Chesney, B. J. Ryan, U. Ramesh, M. G. Panthani and K. J. Cash, *Sens. Actuators, B*, 2021, **331**, 129350.
26 S. Ng and M. Pumera, *Adv. Mater.*, 2023, **35**, 2207196.
27 S. Jiang, M. Q. Arguilla, N. D. Cultrara and J. E. Goldberger, *Acc. Chem. Res.*, 2015, **48**, 144–151.
28 W. L. B. Huey and J. E. Goldberger, *Chem. Soc. Rev.*, 2018, **47**, 6201–6223.
29 B. J. Ryan, M. P. Hanrahan, Y. Wang, U. Ramesh, C. K. A. Nyamekye, R. D. Nelson, Z. Liu, C. Huang, B. Whitehead, J. Wang, L. T. Roling, E. A. Smith, A. J. Rossini and M. G. Panthani, *Chem. Mater.*, 2020, **32**, 795–804.
30 B. J. Ryan, L. T. Roling and M. G. Panthani, *ACS Nano*, 2021, **15**, 14557–14569.
31 S. W. Kim, J. Lee, J. H. Sung, D. Seo, I. Kim, M.-H. Jo, B. W. Kwon, W. K. Choi and H.-J. Choi, *ACS Nano*, 2014, **8**, 6556–6562.
32 N. D. Drummond, V. Zólyomi and V. I. Fal'ko, *Phys. Rev. B: Condens. Matter Mater. Phys.*, 2012, **85**, 75423.
33 A. Stathis, M. Stavrou, I. Papadakis, J. Mock, M. J. Kloberg, M. Becerer, A. Lyuleeva-Husemann and S. Couris, *J. Phys. Chem. C*, 2021, **125**, 18510–18516.

34 H. Imagawa and H. Itahara, *Dalton Trans.*, 2017, **46**, 3655–3660.

35 R. Gao, J. Tang, X. Yu, S. Lin, K. Zhang and L.-C. Qin, *Adv. Funct. Mater.*, 2020, **30**, 2002200.

36 C. Wang, X. Xu, X. Pi, M. D. Butala, W. Huang, L. Yin, W. Peng, M. Ali, S. C. Bodepudi, X. Qiao, Y. Xu, W. Sun and D. Yang, *Nat. Commun.*, 2022, **13**, 5216.

37 Y. You, C. Yang, X. Zhang, H. Lin and J. Shi, *Mater. Today Nano*, 2021, **16**, 100132.

38 F. Wöhler, *Justus Liebigs Ann. Chem.*, 1863, **127**, 257–274.

39 H. Kautsky, *Z. Anorg. Allg. Chem.*, 1921, **117**, 209–242.

40 H. Kautsky and G. Herzberg, *Z. Anorg. Chem.*, 1924, **139**, 135–160.

41 A. Weiss, G. Beil and H. Meyer, *Z. Naturforsch., B*, 1980, **35**, 25–30.

42 J. R. Dahn, B. M. Way, E. Fuller and J. S. Tse, *Phys. Rev. B: Condens. Matter Mater. Phys.*, 1993, **48**, 17872–17877.

43 S. Yamanaka, H. Matsu-ura and M. Ishikawa, *Mater. Res. Bull.*, 1996, **31**, 307–316.

44 K. Nishimura, Y. Nagao, S. Yamanaka and H. Matsu-ura, *Jpn. J. Appl. Phys.*, 1996, **35**, L293.

45 R. W. Dorn, B. J. Ryan, S. N. S. Lamahewage, M. V. Dodson, J. B. Essner, R. Biswas, M. G. Panthani and A. J. Rossini, *Chem. Mater.*, 2023, **35**, 539–548.

46 X. Deng, X. Zheng, T. Yuan, W. Sui, Y. Xie, O. Voznyy, Y. Wang and Z. Yang, *Chem. Mater.*, 2021, **33**, 9357–9365.

47 D. Karar, N. Ratan Bandyopadhyay, A. Kumar Pramanick, D. Acharyya, G. Conibeer, N. Banerjee, O. E. Kusmartseva and M. Ray, *J. Phys. Chem. C*, 2018, **122**, 18912–18921.

48 M. S. Brandt, H. D. Fuchs, M. Stutzmann, J. Weber and M. Cardona, *Solid State Commun.*, 1992, **81**, 307–312.

49 P. Deák, M. Rosenbauer, M. Stutzmann, J. Weber and M. S. Brandt, *Phys. Rev. Lett.*, 1992, **69**, 2531–2534.

50 H. D. Fuchs, M. Stutzmann, M. S. Brandt, M. Rosenbauer, J. Weber and M. Cardona, *Phys. Scr.*, 1992, **1992**, 309.

51 M. Stutzmann, M. S. Brandt, M. Rosenbauer, J. Weber and H. D. Fuchs, *Phys. Rev. B: Condens. Matter Mater. Phys.*, 1993, **47**, 4806–4809.

52 B. J. Ryan, G. Bhaskar, J. B. Essner, A. Bera, R. W. Dorn, Y. Guo, Q. Hua Wang, A. J. Rossini, J. V. Zaikina, L. T. Roling and M. G. Panthani, *ACS Appl. Nano Mater.*, 2023, **6**, 10054–10063.

53 S. Rivillon, F. Amy, Y. J. Chabal and M. M. Frank, *Appl. Phys. Lett.*, 2004, **85**, 2583–2585.

54 B. J. Eves and G. P. Lopinski, *Surf. Sci.*, 2005, **579**, 89–96.

55 F. A. Soria, E. M. Patrito and P. Paredes-Olivera, *J. Phys. Chem. C*, 2013, **117**, 18021–18030.

56 M. F. Juarez, E. M. Patrito and P. Paredes-Olivera, *J. Phys. Chem. C*, 2008, **113**, 681–690.

57 G. Allen Ferguson, S. Rivillon, Y. Chabal and K. Raghavachari, *J. Phys. Chem. C*, 2009, **113**, 21713–21720.

58 R. Wakabayashi, Y. Sugiura, T. Shibue and K. Kuroda, *Angew. Chem., Int. Ed.*, 2011, **50**, 10708–10711.

59 N. Jingu, K. Sumida, T. Hayakawa, T. Ono and K. Saitow, *Chem. Mater.*, 2024, **36**, 5077–5091.

60 P. Zhang, X. D. Li, C. H. Hu, S. Q. Wu and Z. Z. Zhu, *Phys. Lett. A*, 2012, **376**, 1230–1233.

61 M. Houssa, E. Scalise, K. Sankaran, G. Pourtois, V. V. Afanas'ev and A. Stesmans, *Appl. Phys. Lett.*, 2011, **98**, 223107.

62 Y. Ding and Y. Wang, *J. Phys. Chem. C*, 2018, **122**, 23208–23216.

63 P. Miró, M. Audiffred and T. Heine, *Chem. Soc. Rev.*, 2014, **43**, 6537–6554.

64 Á. Morales-García, R. Valero and F. Illas, *J. Phys. Chem. C*, 2017, **121**, 18862–18866.

65 Y. J. Chabal and L. C. Feldman, *Electrochem. Soc. Interface*, 2005, **14**, 31.

66 F. A. Soria, E. M. Patrito and P. Paredes-Olivera, *J. Phys. Chem. C*, 2012, **116**, 24607–24615.

67 X. Zhang, Y. J. Chabal, S. B. Christman, E. E. Chaban and E. Garfunkel, *J. Vac. Sci. Technol., A*, 2001, **19**, 1725–1729.

68 B. Gokce, E. J. Adles, D. E. Aspnes and K. Gundogdu, *Proc. Natl. Acad. Sci. U. S. A.*, 2010, **107**, 17503–17508.